Computational Materials Science 188 (2021) 110201

Contents lists available at ScienceDirect

Computational Materials Science

journal homepage: www.elsevier.com/locate/commatsci

Hardening Ni_3Al via complex stacking faults and twinning boundary

Zhiwei Zhang [a,b], Qiang Fu [c], Jun Wang [a,*], Pan Xiao [a], Fujiu Ke [d], Chunsheng Lu [e]

[a] State Key Laboratory of Nonlinear Mechanics (LNM), Institute of Mechanics, Chinese Academy of Sciences, Beijing 100190, China
[b] School of Engineering Science, University of Chinese Academy of Sciences, Beijing 100049, China
[c] Aero Engine Academy of China, Beijing 101304, China
[d] School of Physics, Beihang University, Beijing 100191, China
[e] School of Civil and Mechanical Engineering, Curtin University, Perth, WA 6845, Australia

ARTICLE INFO

Keywords:
Ni_3Al
Complex stacking faults
Hardness
Twinning boundary
Molecular dynamics

ABSTRACT

Introducing nanoscale planar defects instead of adding alloying elements has been applied to improve the mechanical properties of materials. In this paper, we show that, from an atomistic perspective, hardness of nickel aluminide (Ni_3Al) can be effectively enhanced by complex stacking faults and twinning boundary. The size effect of planar defects is induced by a competition between hardening because of regeneration of stacking faults and softening due to detwinning. The complex stacking faults have a better hardening effect than twinning boundaries with a spacing below 3.0 nm. These findings provide new insights into nanostructural design of aerospace materials with high hardness.

1. Introduction

Alloying metals and nanostructured materials with defects exhibit exceptional mechanical and physical properties that are promising in various applications [1–6]. As is known, alloying is usually applied to improve materials; however, it is more dependent on resources and not conducive to recycling and re-utilization. In contrast, by adjusting defects inside a material, nanoscale microstructural design can sustainably enhance its properties [7–10]. It is shown that planar defects like twinning boundary (TB) can simultaneously increase the hardness and stability of nanostructured diamond and cubic boron nitride [11,12], as well as other metallic materials [13–15]. Whereas, it is unclear whether stacking faults, another kind of common planar defect, can increase hardness of materials. To the best of our knowledge, there is still lack of studies on how stacking faults affect hardness of nanostructured materials.

Nickel aluminide (Ni_3Al) is an intermetallic ordered alloy with the $L1_2$ structure. It has been widely applied in aerospace industries such as turbine blades and vanes in aircraft engines. However, a lower susceptibility to plastic deformation and a higher tendency to brittle cracking strongly limit its industrial applications [16–18]. To elucidate mechanisms of deformation and hardness of single crystal Ni_3Al (SC-Ni_3Al), extensive nanoindentation experiments and numerical simulations have been performed on, e.g., effects of crystallographic orientation, temperature, indenter radius and incipient plasticity [19–25]. It is found out that the super-lattice structure of Ni_3Al leads to a complexity of microstructures and consequently diverse modes of deformation. Depending on atomic arrangements in the $L1_2$ structure, there are two typical kinds of intrinsic planar defects in Ni_3Al such as complex stacking faults (CSFs) and TBs [26,27]. Studying these planar defects is significant to a better understanding of hardness of nanostructured Ni_3Al. Here, it is worth noting that the size of planar defects plays a major role in tuning dislocation activities, which drastically affects the hardness of $L1_2$ Ni_3Al.

In this paper, we introduced CSFs into Ni_3Al to investigate whether such configurations could harden Ni_3Al substrate in comparison with TBs. By using molecular dynamic simulations, a series of SC-Ni_3Al, CSF-Ni_3Al, and TB-Ni_3Al were modeled under nanoindentation with various spacings between parallel planar defects (hereafter referred to as the spacing). The size effect of planar defects on hardness and corresponding deformation mechanism at the atomistic level have been investigated.

2. Methods

2.1. Nanostructured Ni_3Al models

Generally, SC-, CSF- and TB-Ni_3Al models were established on the fact that Ni_3Al is a close-packed structure with an arrangement of three

* Corresponding author.
E-mail address: wangjun@lnm.imech.ac.cn (J. Wang).

https://doi.org/10.1016/j.commatsci.2020.110201
Received 18 October 2020; Received in revised form 17 November 2020; Accepted 18 November 2020
Available online 10 December 2020

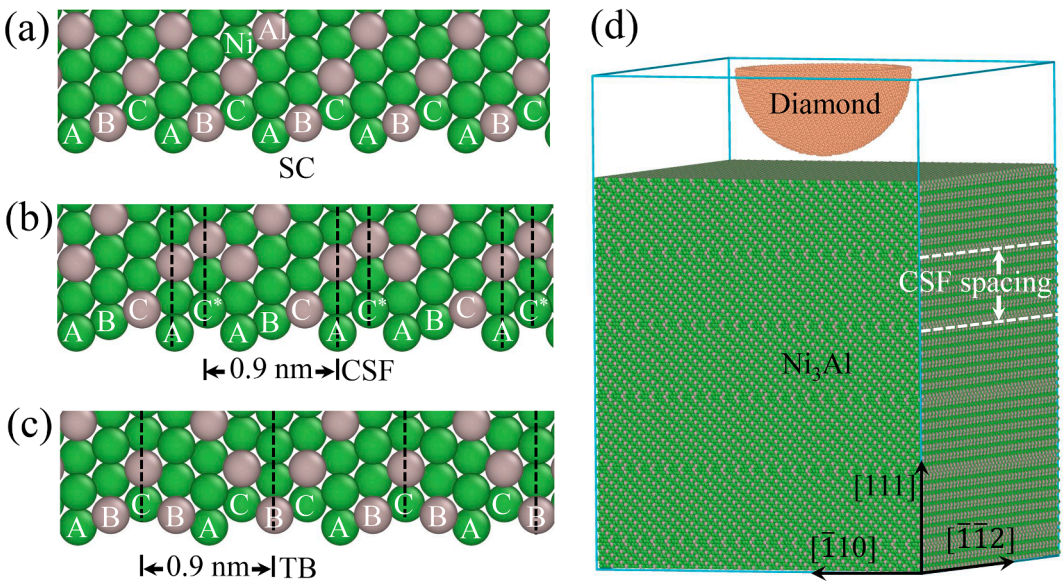

Fig 1. The stacking sequence of nanostructured $L1_2$ Ni_3Al in (a) SC, (b) CSF and (c) TB with a spacing of 0.9 nm between parallel planar defects. (d) Sketch of a nanoindentation model for CSF-Ni_3Al with a spacing of 3.9 nm between parallel CSFs.

successive planes, denoting as A, B and C, along the [111] direction (see Fig. 1a–c, which is also Fig. S1 for clarity of the supplementary data). Here, SC-Ni_3Al models consist of periodically reproducing the ABC stacking sequence. Considering planar defects, a system should contain at least one ABC unit to keep integrity of the $L1_2$ crystal structure. This gives the lower limit of a spacing, i.e., 0.9 nm. Specifically, CSF-Ni_3Al models were formed by shearing C with $a/6[11\bar{2}]$ (111), with a being the lattice constant of Ni_3Al. That is, CSF-Ni_3Al with a spacing of 0.9 nm corresponds to a stacking sequence of ***AC****ABC as a periodically repeating unit, where bold and italic letters represent planar defects. Here, the layer ***C**** adopts an alternatively atomic arrangement in contrast to the layer C of SC-Ni_3Al [26]. The corresponding periodic stacking sequence of TB-Ni_3Al with a spacing of 0.9 nm is ***C***BAC***B***CAB. Fig. 1d shows an initial configuration of CSF-Ni_3Al with a spacing of 3.9 nm for indentation simulation. All Ni_3Al substrates were created in a cubic shape with a size of 20 × 20 × 22 nm^3 along the X-$[1\bar{1}0]$, Y-$[11\bar{2}]$ and Z-[111] directions, containing ~ 800,000 atoms. A hemisphere shell diamond indenter was used with a diameter of 10 nm (~20,000 atoms). During indentation, periodic boundary conditions were introduced in the X and Y crystallographic directions. The top surface was chosen as the one under indentation, while the region was fixed at bottom with a thickness of 1.0 nm.

2.2. Molecular dynamics simulations

For CSF- and TB-Ni_3Al models, eight samples were simulated with various spacings (i.e., 0.9, 1.5, 2.1, 2.7, 3.9, 5.2, 6.4 and 10.7 nm). The SC-Ni_3Al substrate was taken as a reference to investigate hardening effect of TBs and CSFs. Atomistic simulations were performed by using the Largescale Atomic/Molecular Massively Parallel Simulator [28]. The embedded-atom potential function for a Ni–Al system developed by Mishin [29] was taken to define the atomic interaction of Ni_3Al. In this function, the total energy, E, of a system can be described as

$$E = \sum_{\substack{i,j \\ i\neq j}} V_{EAM}(r_{ij}) + \sum_{i} F(\overline{\rho_i}) \tag{1}$$

where $V_{EAM}(r_{ij})$ is a pair potential represented as a function of the distance r_{ij} between atoms i and j, and F is the embedding energy of atom i, and $\overline{\rho_i}$ is the electron density, which is given by

Table 1
Lennard-Jones potential function parameters for C–Ni and C–Al [30,31].

Parameters	C–Ni	C–Al
σ_{ij}, Equilibrium distance (nm)	0.2852	0.2976
ε_{ij}, Cohesive energy (10^{-3} eV)	23.1	31.5
r_0, Cutoff distance (nm)	0.8	0.8

$$\overline{\rho_i} = \sum_{i\neq j} g_j(r_{ij}) \tag{2}$$

where $g_j(r_{ij})$ is the electron density of atom j.

The force between a diamond indenter and substrate was described with a two-body Lennard-Jones potential function,

$$E = 4\sum_{\substack{i,j \\ i\neq j}} \varepsilon_{ij}\left[\left(\frac{\sigma_{ij}}{r_{ij}}\right)^{12} - \left(\frac{\sigma_{ij}}{r_{ij}}\right)^{6}\right], r_{ij} < r_0 \tag{3}$$

where ε_{ij} is cohesive energy; σ_{ij} is the equilibrium distance and r_0 is the cutoff distance [30,31]. Their values are listed in Table 1.

Simulations were carried out by integrating Newton's equations of motion for all atoms with a time step of 1 fs. At the start of simulation, initial configurations were energetically minimized by relaxing all samples for 50 ps at 300 K. To obtain hardness of nanostructural Ni_3Al, an indentation load was applied along the Z direction (perpendicular to planes of CSFs and TBs). The indentation speed and step increment were 10 m s^{-1} and 5.0 × 10^{-2} nm, respectively. The maximum indentation depth was 4.0 nm, smaller than the diameter of indenter. Deformation and defects of Ni_3Al substrate were recognized via the common neighbor and dislocation analysis and then, they were visualized with software OVITO [32].

2.3. Determining volume of plastic zones

To assess the relative constraint of planar defects to expanding of a plastic zone, we resort to the Taylor relationship in which hardness (H) can make a connection with the dislocation density (δ) by

$$H = MC\alpha Gb\sqrt{\delta} \tag{4}$$

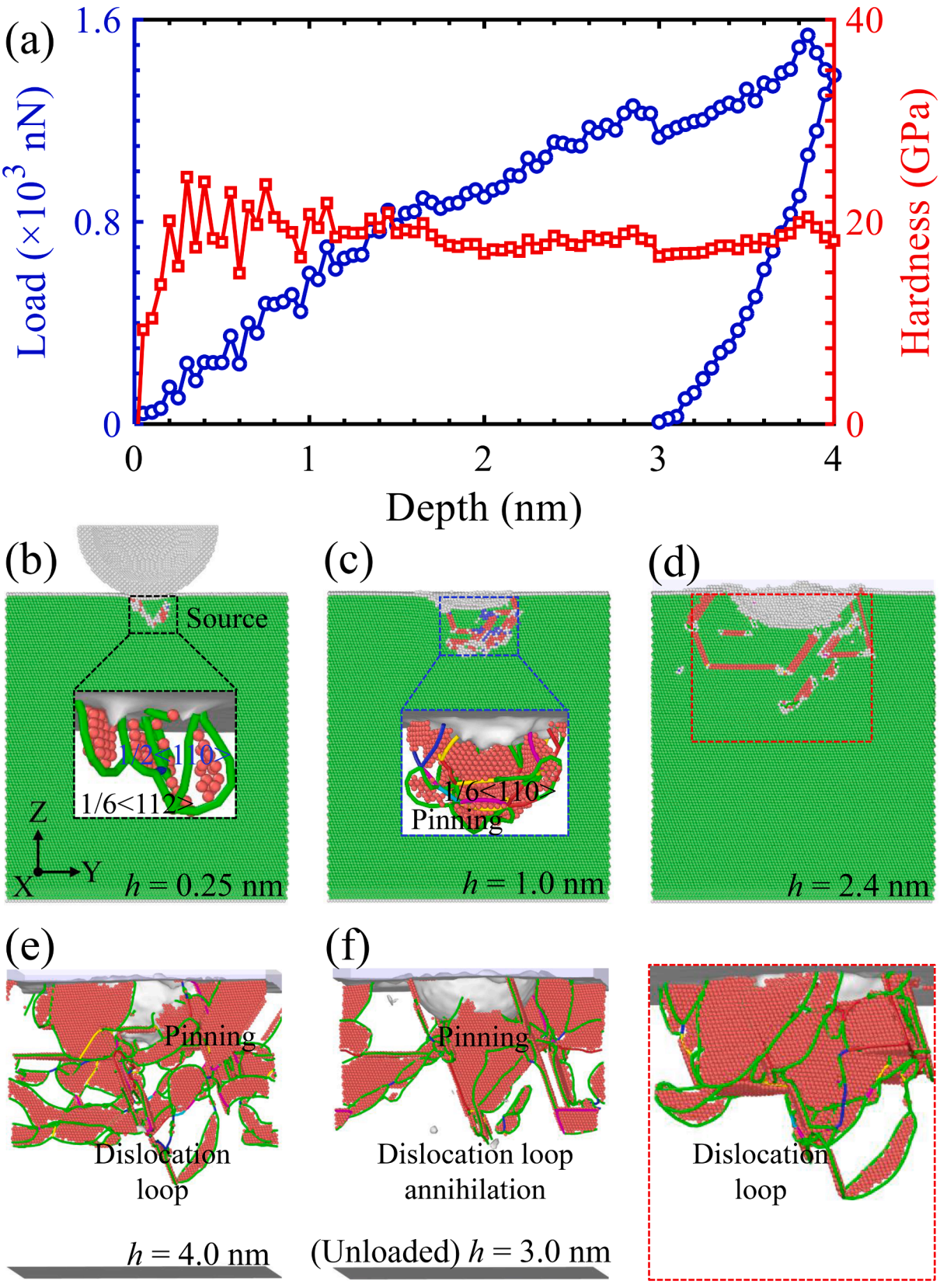

Fig 2. (a) Typical indentation load/hardness-depth relationships of SC-Ni_3Al and the atomic configurations of an SC-Ni_3Al at various indentation depths of (b) 0.25 nm, (c) 1.0 nm, (d) 2.4 nm, (e) 4.0 nm and (f) 3.0 nm (unloaded), where atoms were colored by common neighbor and dislocation analysis. Insets in (b)–(d) show structures of local dislocations visualized by dislocation analysis with green, blue, purple, yellow and red lines indicating 1/6⟨112⟩ Shockley, 1/2⟨110⟩ perfect, 1/6⟨110⟩ stair-rod, 1/3⟨100⟩ Hirth, and other kind of dislocations, respectively. FCC structures were removed for clarity in (e) and (f).

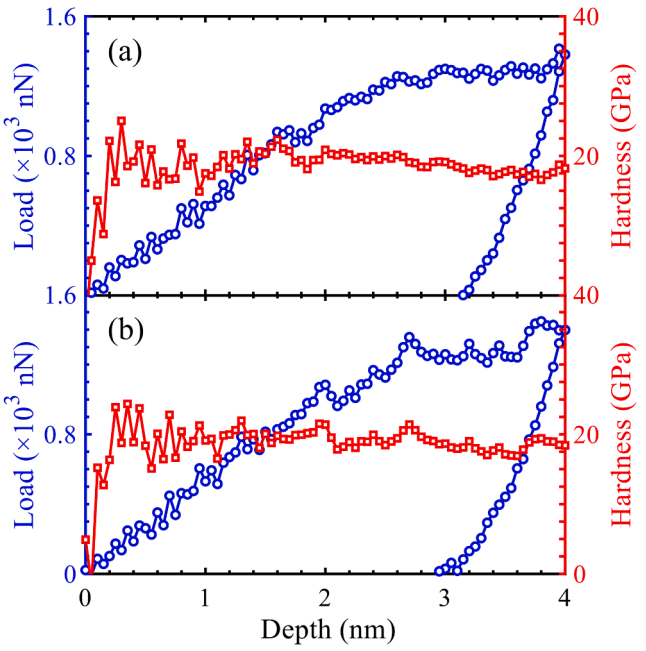

Fig 3. Indentation load/hardness-depth relationships of (a) TB-Ni_3Al and (b) CSF-Ni_3Al with a spacing of 3.9 nm between parallel defects.

where M is the Taylor factor, C represents constraint imposed by the elastically deformed area surrounding an indenter, α is a constant, G is the shear modulus, and b is Burgers vector [33].

In simulations, the 1/6⟨112⟩ Shockley dislocation accounts for an overwhelming percentage, thus we assume that there is only one value for b. Here, let $MC\alpha Gb = k$ (k can be regarded as a constant), and then Eq. (4) can be simplified to

$$H = k \times \sqrt{\frac{L}{V}} \tag{5}$$

where L and V indicate the total length of dislocation lines and the volume of a plastic zone, respectively. By selecting V of SC-Ni_3Al as a reference, the volumes of TB-Ni_3Al and CSF-Ni_3Al can be subsequently determined according to Eq. (5) since L can be directly measured by dislocation analysis.

3. Results

3.1. Deformation mechanisms of SC-Ni_3Al

As shown in Fig. 2a, there is an upward trend with many slight drops or fluctuations in a typical indentation load-depth curve, corresponding to multiple dislocation events, until the ultimate depth of 4.0 nm. Subsequently, with the indenter retracted by 1.0 nm, load gradually decreases to 0 GPa at a depth of 3.0 nm. However, the hardness-depth curve increases sharply at the beginning and reaches the peak value of 24.5 GPa. Then, it gradually fluctuates and tends to be stable. Hardness of SC-Ni_3Al was measured as 18.1 GPa, which is an average value between indentation depths of 2.0–4.0 nm and the same strategy was adopted to characterize hardness of nanostructural Ni_3Al.

To clarify the deformation mechanism of SC-Ni_3Al, microstructures with various depths (h) were extracted by using the common neighbor and dislocation analysis (see Fig. 2b–f). At a depth of 0.25 nm, a few 1/6⟨112⟩ Shockley dislocations nucleate on the surface of SC-Ni_3Al substrate beneath the indenter, and then a 1/2⟨110⟩ perfect dislocation emerges to pin dislocations (Fig. 2b). Further, with depth increasing, more 1/6⟨112⟩ Shockley dislocations (accounting for 57.4% density of dislocation lines) nucleate below the surface and propagate inward. Reaction between 1/6⟨112⟩ Shockley dislocations forms 1/6⟨110⟩ stair-rod dislocations (with a density of 6.4%) at their junction areas, which results in dislocation pinning (Fig. 2c). As depth reaches 2.4 nm, 1/6⟨112⟩ Shockley dislocations continuously nucleate, grow, slip and interact, generating dislocation loops at deeper positions in Ni_3Al substrate (Fig. 2d). Further increase in depth induces more dislocation activities as shown in Fig. 2e. At the depth of 4.0 nm, dislocations in SC-Ni_3Al substrate are mainly 1/6⟨112⟩ (accounting for 77.1%), together with a small amount of 1/6⟨110⟩ stair-rod, 1/3⟨100⟩ Hirth, 1/3⟨111⟩ perfect and 1/2⟨110⟩ perfect. Finally, as the indenter retracts from 4.0 nm to 3.0 nm, annihilation and contraction of dislocation loops are seen with the length of dislocation lines reducing from 9.7×10^2 to 5.3×10^2 nm (see Fig. 2e and f).

3.2. Effects of the spacing between planar defects

The typical curves of indentation load (hardness) versus depth in TB-Ni_3Al and CSF-Ni_3Al are illustrated in Fig. 3a and b, with a spacing of 3.9 nm between parallel defects. It is shown that, in contrast to SC, nanostructures such as TBs and CSFs improve hardness of Ni_3Al, as summarized in Fig. 4a. Specifically, hardness of CSF-Ni_3Al increases from 18.1 GPa (the same as that of SC-Ni_3Al) to 19.0 GPa as spacing decreases from 10.7 nm to 2.1 nm, indicating the Hall-Petch effect. However, hardness of CSF-Ni_3Al falls to 18.1 GPa with the spacing further decreasing to 0.9 nm, exhibiting the inverse Hall-Petch effect. For TB-Ni_3Al, the maximal value of hardness, 19.1 GPa, is attained at a spacing of 5.2 nm. The similar inverse Hall-Petch effect was also observed with a lower spacing. Here it is worth noting that hardness of CSF-Ni_3Al or TB-Ni_3Al is beyond that of SC-Ni_3Al. Moreover, CSFs have a stronger hardening effect with a spacing less than 3.0 nm, while TBs are in the lead with a spacing more than this value (see Fig. 4a).

As shown in Fig. 4b, the volume of a plastic zone is strongly

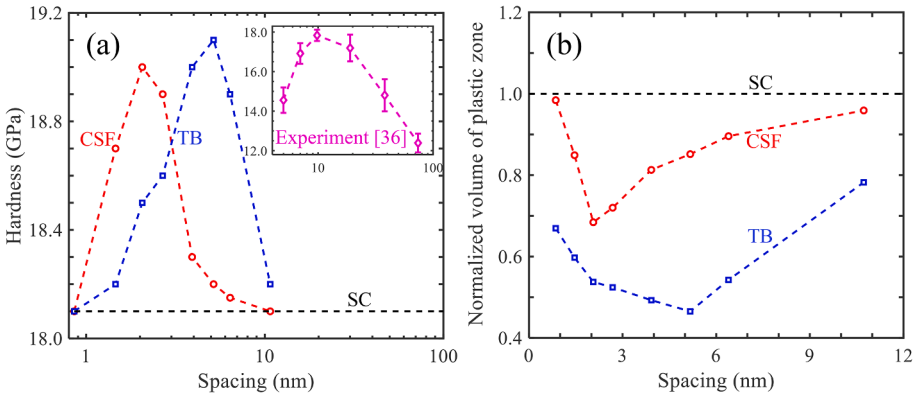

Fig 4. (a) Hardness of nanostructured Ni_3Al and (b) normalized volume of plastic zones versus spacing between parallel planar defects.

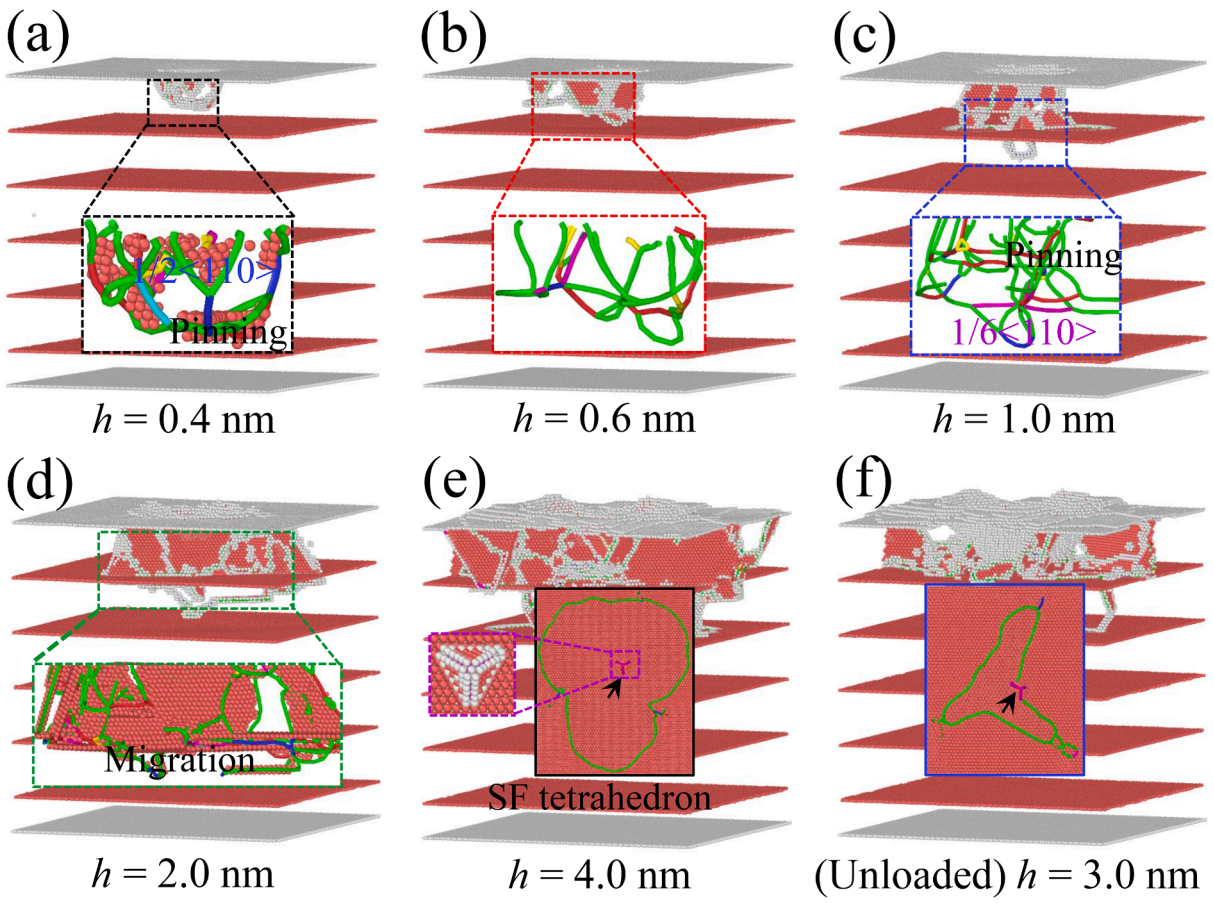

Fig 5. Evolution of microstructures in TB-Ni_3Al with a spacing of 3.9 nm between parallel TBs at various indentation depths of (a) 0.4 nm, (b) 0.6 nm, (c) 1.0 nm, (d) 2.0 nm, (e) 4.0 nm and (f) 3.0 nm (unloaded), where atoms were colored by dislocation analysis with FCC structures removed for clarity. Insets in (a)–(d) show structures of local dislocations. Insets with black and blue edges represent the bottom views below the second TB layer in (e) and (f), respectively. Black arrows mark SF tetrahedrons. Inset with a purple dashed edge in (e) shows the three-dimensional structure of SF tetrahedron.

dependent on spacing. The plastic zone volume of CSF-Ni_3Al decreases to its minimum, as spacing increases from 0.9 nm to 2.1 nm, and then, it increases and closes to the corresponding value of SC-Ni_3Al with spacing rising to 10.7 nm. For TB-Ni_3Al, there is a similar trend, and the volume firstly reduces as spacing decreases from 10.7 to 5.2 nm. Then, it climbs as spacing is reduced to 0.9 nm. This is just opposite to that of hardness, and as shown in Fig. 4a, the volumes of plastic zones and hardness reach their minimum and maximum values at the same spacing, respectively.

3.3. Deformation mechanisms of TB-Ni_3Al

To understand the hardening effect, dislocation activities were monitored. Fig. 5 shows atomic configurations of deformed TB-Ni_3Al with a spacing of 3.9 nm during indentation. Dislocations first nucleate on indentation surface beneath the indenter and then spread inward in Ni_3Al substrate. Several $1/6\langle 112\rangle$ Shockley dislocations continuously grow, slip and interact, forming a $1/2\langle 110\rangle$ perfect dislocation to pin a small amount of $1/6\langle 112\rangle$ Shockley dislocations (Fig. 5a). Then, with depth increasing, several $1/6\langle 112\rangle$ Shockley dislocations spread down and meet the first TB layer (Fig. 5b). As dislocations move to TB, they are impeded and react with TB. Reaction brings $1/6\langle 110\rangle$ stair-rod, $1/2\langle 110\rangle$ perfect and $1/3\langle 100\rangle$ Hirth dislocations, accounting for the density of dislocation lines of 9.2%, 5.3% and 4.1%, respectively (see Fig. 5c). Reaction also sets off migration of TB as shown in Fig. 5d. As TB migrates downward, the pinning effect was observed above it. Dislocations participating pinning are mainly $1/6\langle 112\rangle$ Shockley (61.5%) and a small amount of $1/6\langle 110\rangle$ stair-rod, $1/3\langle 100\rangle$ Hirth, $1/3\langle 111\rangle$ Frank and $1/2\langle 110\rangle$ perfect. With depth increasing to 4.0 nm, dislocations move to the second TB layer, where they are obstructed and interact with TB. Reaction of dislocations results in an SF tetrahedron in the middle of the second TB layer (see Fig. 5e). Finally, as shown in Fig. 5f, with the indenter retracting to a depth of 3.0 nm, the length of dislocation lines in Ni_3Al substrate reduces from 5.3×10^2 to 2.6×10^2 nm due to stress release. Meanwhile, the $1/6\langle 112\rangle$ Shockley dislocation loop on the second TB layer gradually contract and the SF tetrahedron is left on the second TB layer. Supplementary Movie. 1 offers structural evolution of TB-Ni_3Al with the spacing of 3.9 nm during indentation process.

3.4. Deformation mechanisms of CSF-Ni_3Al

For a comparison, the microstructural evolution of a CSF-Ni_3Al with a spacing of 3.9 nm is shown in Fig. 6. At a depth of 0.25 nm, several $1/6\langle 112\rangle$ Shockley dislocations nucleate on surface of Ni_3Al substrate and spread inward. Interaction between $1/6\langle 112\rangle$ Shockley dislocations leads to formation of $1/2\langle 110\rangle$ perfect dislocations at their junction areas. The interaction pins a small amount of $1/6\langle 112\rangle$ dislocations below the indenter (Fig. 6a). Then, with depth increasing, unpinned $1/6\langle 112\rangle$ dislocations propagate downwards and meet the first CSF. Such an activity stimulates a $1/6\langle 112\rangle$ Shockley dislocation loop on the CSF in-plane. Transverse propagation of the stimulated $1/6\langle 112\rangle$ dislocation loop causes fading of CSF. Subsequently, the entire first CSF layer is faded directly (see Fig. 6b). However, as depth increases to 0.95 nm, part of the first CSF layer is regenerated (see Fig. 6c). At this moment, due to impediment of the first CSF, all dislocations in Ni_3Al substrate exist above the first CSF layer without propagating downward. Then, with depth further increasing to 2.0 nm, $1/6\langle 112\rangle$ dislocations pass through

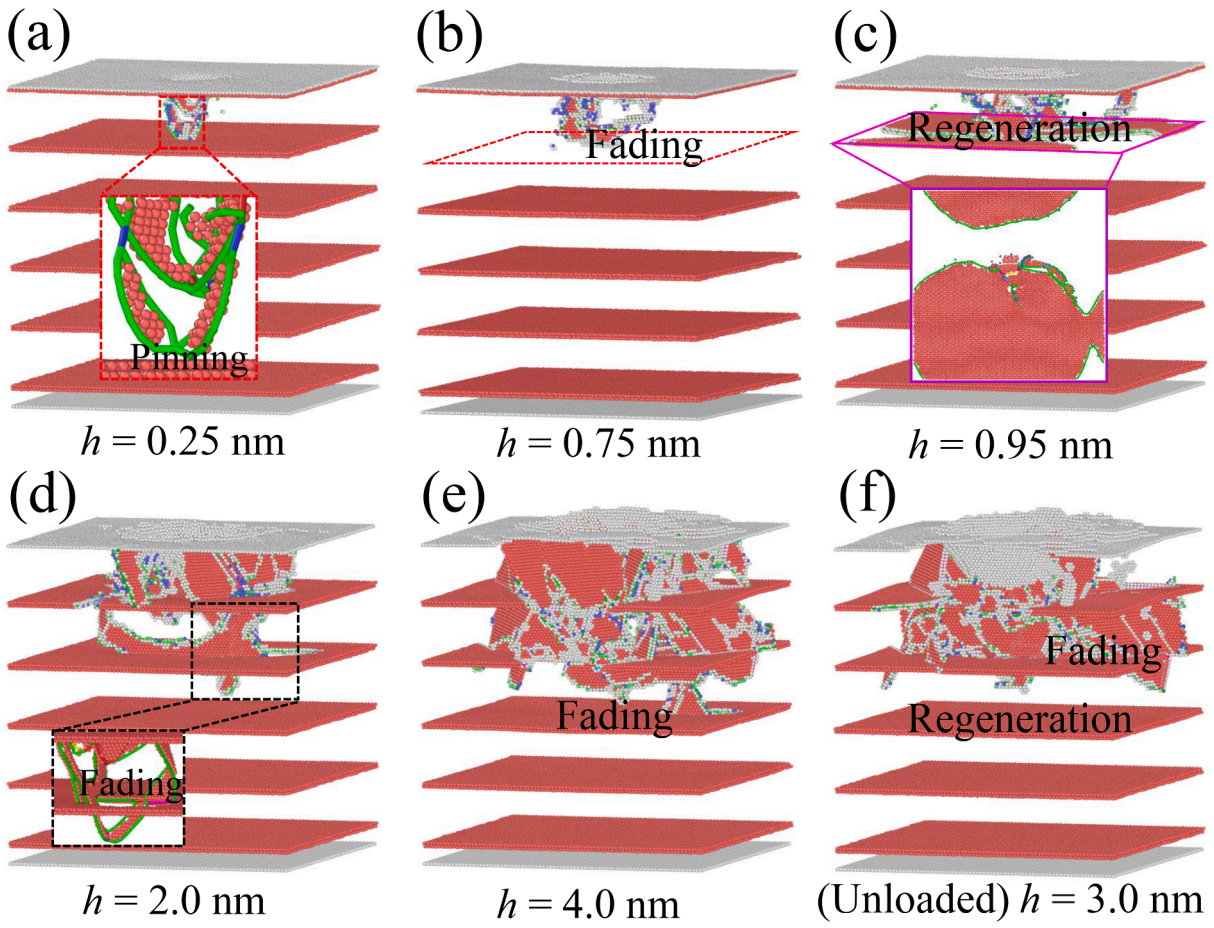

Fig 6. Configurations were analyzed by dislocation analysis in CSF-Ni_3Al with a spacing of 3.9 nm between parallel CSFs at various indentation depths of (a) 0.25 nm, (b) 0.75 nm, c 0.95 nm, (d) 2.0 nm, (e) 4.0 nm and (f) 3.0 nm (unloaded). Insets in (a) and (d) show structures of local dislocations. The red dashed parallelogram in (b) represents the faded first CSF. Bottom view below the first CSF layer in (c) is shown in inset with purple solid edges.

the first CSF layer and propagate downward, contacting and interacting with the second CSF layer, resulting in partial fading of the second CSF (see Fig. 6d). However, a 1/6⟨110⟩ stair-rod dislocation is formed at the edge of the faded part of the second CSF layer (see amplified regions in Fig. 6d). The 1/6⟨110⟩ stair-rod hinders further fading of the second CSF. With depth increasing to 4.0 nm, dislocations continue to spread, multiply, pining and interact with each other. Meanwhile, fading and regeneration of CSFs emerge ceaselessly (Fig. 6e). Dislocations participating pinning are mainly 1/6⟨112⟩ Shockley (66.1%), 1/6⟨110⟩ stair-rod (11.9%), and a small amount of 1/3⟨111⟩ Frank, 1/3⟨100⟩ Hirth and 1/2⟨110⟩ perfect. After retraction, the faded part of the third CSF layer is completely regenerated (Fig. 6f). Here it is worth noting that fading and regeneration of CSF are independent of the spacing. Supplementary Movie. 2 provides structural evolution of CSF-Ni_3Al with the spacing of 3.9 nm.

4. Discussions

As mentioned above, the volume of a plastic zone and hardness of nanostructural Ni_3Al significantly depend on spacing. At the critical value of spacing, hardness approaches its maximum while the volume of a plastic zone falls to its minimum. Beyond this value, hardness follows the Hall-Petch relationship since the plastic zone is restricted by planar defects. However, the inverse Hall-Petch relationship emerges below the critical spacing because planar defects cannot constrain plastic zones. The trend of hardness is well consistent with that in hierarchically nanotwinned FCC metals [34], Cu/Ni nanotwinned multilayer films [35] and Ni_3Al/Ni multilayers [36]. The discrepancy between values of hardness mainly results from the two facts: one is pure Ni_3Al and the other is the shape of a hemisphere indenter with a diameter of 10.0 nm in our work. However, the Berkovich indenter was used for Ni_3Al/Ni multilayers [36]. It has been confirmed that hardness varies with the size and shape of an indenter [23]. In addition, since hardness is a measure of materials for their resisting plastic deformation, a smaller plastic zone produces a higher hardness. This explains the opposite trend between the volume of a plastic zone and hardness.

Planar defects result in hardening and softening. The former includes impediment of planar defects to propagation of dislocations, pinning of dislocations and regeneration of CSFs. The latter consists of detwinning, migration of TBs and fading of CSFs. Specifically, For TB-Ni_3Al, as spacing is less than 5.2 nm, softening mechanisms, such as detwinning and migration of TBs, dominate deformation of plastic zones (see Fig. S2a–d for deformed atomic configurations in TB-Ni_3Al with spacing of 0.9 nm and 6.4 nm, respectively). Beyond 5.2 nm, hardening deformation mechanisms include impediment of TBs to propagation of dislocations, pinning of dislocations at a local region. This is consistent with results measured from nanotwinned Cu [34]. However, softening and hardening mechanisms by CSFs are different from that of TBs. The critical value of spacing is 2.1 nm. Below this value, the softening mechanism results from fading of the entire layer of CSFs (see Fig. S3a and b for deformed atomic configurations of CSF-Ni_3Al with a spacing of 0.9 nm). Beyond 2.1 nm, deformation is dominated by hardening mechanisms such as impediment of CSFs to propagation of dislocations, pinning of dislocations and partial regeneration of CSFs (see Fig. S3c and d for configurations of CSF-Ni_3Al with a spacing of 6.4 nm at various indentation depths). Applying SFs to improve strength has been realized

in Mg alloys [37–39] and other metals [40]. Since hardness roughly increases with the increase of strength, this provides an indirect evidence for hardening materials by SFs. In contrast, SC-Ni_3Al without planar defects produces a lower hardness due to lack of microstructures to offer hardening mechanisms to restrict development of plastic zones.

It is of interest to note that CSF-Ni_3Al and TB-Ni_3Al generate the same hardness of 18.7 GPa at a spacing of 3.0 nm (see Fig. 4a). This is because when hardening mechanisms play a role in CSF-Ni_3Al, softening factors take over deformation of TB-Ni_3Al, with the reduction of spacing. It is shown that, at a spacing of 3.0 nm, TBs lose control on development of a plastic zone, which undergoes a rise with the decrease of spacing. However, the volume of a plastic zone in CSF-Ni_3Al still follows a reducing trend at the same spacing range. That is, competition between softening and hardening results in a better hardening effect of CSFs than TBs with a spacing below 3.0 nm, and vice versa.

5. Conclusions

Hardness of nanostructural Ni_3Al has been investigated under nanoindentation by a series of molecular dynamics simulations, with spacing between parallel planar defects being a key variable. It is shown that, hardening can be achieved by planar defects such as CSFs and TBs with SC as a reference. The conclusions are as follows:

(1) There is the same hardness of CSFs and TBs at a critical spacing of 3.0 nm between parallel planar defects. Below the spacing value, the hardening effect of CSFs is stronger than TBs.
(2) Hardening factors are attributed to impediment of planar defects to propagation of dislocations, regeneration of CSFs and pinning effect resulting from the interaction between dislocations and planar defects.
(3) Softening aspects include fading of CSFs, detwinning and migration of TBs.

These findings provide new insights into a deep understanding on deformation mechanisms of nanostructured Ni_3Al and benefit its optimal design and wide applications in aerospace industries.

6. Data availability

The data that support the findings within this paper are available from the corresponding authors upon reasonable request.

CRediT authorship contribution statement

Zhiwei Zhang: Investigation, Methodology, Data curation, Writing - original draft. **Qiang Fu:** Formal analysis. **Jun Wang:** Conceptualization, Supervision, Writing - review & editing, Funding acquisition. **Pan Xiao:** Funding acquisition, Methodology. **Fujiu Ke:** Conceptualization, Writing - review & editing. **Chunsheng Lu:** Writing - review & editing.

Declaration of Competing Interest

The authors declare that they have no known competing financial interests or personal relationships that could have appeared to influence the work reported in this paper.

Acknowledgements

This work has been supported by the National Natural Science Foundation of China (Grant Nos. 11772332 and 11790292), the Strategic Priority Research Program of the Chinese Academy of Sciences (Project No. XDB22040501), and the Opening Fund of State Key Laboratory of Nonlinear Mechanics. The simulations were performed on resources provided by the Pawsey Supercomputing Center with funding from the Australian Government and the Government of Western Australia, the ScGrid of Supercomputing Center, Computer Network Information Center of the Chinese Academy of Sciences, and the LNMGrid of the State Key Laboratory of Nonlinear Mechanics.

Appendix A. Supplementary data

Supplementary data to this article can be found online at https://doi.org/10.1016/j.commatsci.2020.110201.

References

[1] I.A. Ovid'Ko, R.Z. Valiev, Y.T. Zhu, Review on superior strength and enhanced ductility of metallic nanomaterials, Prog. Mater. Sci. 94 (2018) 462–540.
[2] M.A. Meyers, A. Mishra, D.J. Benson, Mechanical properties of nanocrystalline materials, Prog. Mater. Sci. 51 (4) (2006) 427–556, https://doi.org/10.1016/j.pmatsci.2005.08.003.
[3] Y.T. Zhu, X.Z. Liao, X.L. Wu, Deformation twinning in nanocrystalline materials, Prog. Mater. Sci. 57 (2012) 1–62.
[4] T. Chookajorn, H.A. Murdoch, C.A. Schuh, Design of Stable Nanocrystalline Alloys, Science 337 (2012) 951–954.
[5] P. Sathiyamoorthi, H.S. Kim, High-entropy alloys with heterogeneous microstructure: processing and mechanical properties, Progr. Mater. Sci. (2020) 100709, https://doi.org/10.1016/j.pmatsci.2020.100709.
[6] X.W. Li, T. Shi, B. Li, X.C. Chen, C.W. Zhang, Z.G. Guo, Q.X. Zhang, Subtractive manufacturing of stable hierarchical micro-nano structures on AA5052 sheet with enhanced water repellence and durable corrosion resistance, Mater. Des. 183 (2019), 108152.
[7] X.W. Li, J.S. Liang, T. Shi, D.N. Yang, X.C. Chen, C.W. Zhang, Z.H. Liu, D.Z. Liu, Q. X. Zhang, Tribological behaviors of vacuum hot-pressed ceramic composites with enhanced cyclic oxidation and corrosion resistance, Ceram. Int. 46 (2020) 12911–12920.
[8] X.Y. Li, K. Lu, Improving sustainability with simpler alloys, Science 364 (2019) 733–734.
[9] F. Shuang, K.E. Aifantis, Relating the strength of graphene/metal composites to the graphene orientation and position, Scr. Mater. 181 (2020) 70–75.
[10] B.K. Reck, T.E. Graedel, Challenges in Metal Recycling, Science 337 (2012) 690–695.
[11] Q. Huang, D.L. Yu, B. Xu, W.T. Hu, Y.M. Ma, Y.B. Wang, Z.S. Zhao, B. Wen, J.L. He, Z.Y. Liu, Y.J. Tian, Nanotwinned diamond with unprecedented hardness and stability, Nature 510 (2014) 250–253.
[12] Y.J. Tian, B. Xu, D.L. Yu, Y.M. Ma, Y.B. Wang, Y.B. Jiang, W.T. Hu, C.C. Tang, Y. F. Gao, K. Luo, Z.S. Zhao, L.M. Wang, B. Wen, J.L. He, Z.Y. Liu, Ultrahard nanotwinned cubic boron nitride, Nature 493 (2013) 385–388.
[13] F. Shuang, K.E. Aifantis, Dislocation-graphene interactions in Cu/graphene composites and the effect of boundary conditions: a molecular dynamics study, Carbon 172 (2021) 50–70.
[14] A.K. Agrawal, A. Singh, A. Vivek, S. Hansen, G. Daehn, Extreme twinning and hardening of 316L from a scalable impact process, Mater. Lett. 225 (2018) 50–53.
[15] H.D. Fan, Y.X. Zhu, J.A. El-Awady, D. Raabe, Precipitation hardening effects on extension twinning in magnesium alloys, Int. J. Plast. 106 (2018) 186–202.
[16] X.Y. Yang, W.Y. Hu, The alloying element dependence of the local lattice deformation and the elastic properties of Ni_3Al: a molecular dynamics simulation, J. Appl. Phys. 115 (2014), 153507.
[17] R. Maaß, L. Meza, B. Gan, S. Tin, J.R. Greer, Ultrahigh strength of dislocation-free Ni_3Al nanocubes, Small 8 (2012) 1869–1875.
[18] P. Jozwik, W. Polkowski, Z. Bojar, Applications of Ni_3Al based intermetallic alloys–current stage and potential perceptivities, Materials 8 (2015) 2537–2568.
[19] W. Wang, C.B. Jiang, K. Lu, Deformation behavior of Ni_3Al single crystals during nanoindentation, Acta Mater. 51 (2003) 6169–6180.
[20] W. Wang, K. Lu, Nanoindentation measurement of hardness and modulus anisotropy in Ni_3Al single crystals, J. Mater. Res. 17 (2002) 2314–2320.
[21] R. Seymour, A. Hemeryck, K.-I. Nomura, W. Wang, R.K. Kalia, A. Nakano, P. Vashishta, Nanoindentation of NiAl and Ni 3 Al crystals on (100), (110), and (111) surfaces: a molecular dynamics study, Appl. Phys. Lett. 104 (14) (2014) 141904, https://doi.org/10.1063/1.4867168.
[22] A. Sawant, S. Tin, High temperature nanoindentation of a Re-bearing single crystal Ni-base superalloy, Scr. Mater. 58 (2008) 275–278.
[23] M. Göken, M. Kempf, Microstructural properties of superalloys investigated by nanoindentations in an atomic force microscope, Acta Mater. 47 (1999) 1043–1052.
[24] K. Xiong, H.M. Lu, J.F. Gu, Atomistic simulations of the nanoindentation-induced incipient plasticity in Ni_3Al crystal, Comput. Mater. Sci. 115 (2016) 214–226.
[25] P.C. Wo, A.H.W. Ngan, Y.L. Chiu, TEM measurement of nanoindentation plastic zones in Ni_3Al, Scr. Mater. 55 (2006) 557–560.
[26] Y.F. Wen, J. Sun, J. Huang, T. First–principles study of stacking fault energies in Ni3Al intermetallic alloys, T. Nonferr. Metal. Soc. 22 (2012) 661−664.
[27] X.X. Yu, C.Y. Wang, The effects of alloying elements on generalized stacking fault energies, strength and ductility of γ'-Ni_3Al, Mater. Sci. Eng. A 539 (2012) 38–41.
[28] S. Plimpton, Fast Parallel Algorithms for Short-Range Molecular Dynamics, J. Comput. Phys. 117 (1995) 1–19.
[29] Y. Mishin, Atomistic modeling of the γ and γ'-phases of the Ni–Al system, Acta Mater. 52 (2004) 1451–1467.

[30] P. Peng, G.L. Liao, T.L. Shi, Z.R. Tang, Y. Gao, Molecular dynamic simulations of nanoindentation in aluminum thin film on silicon substrate, Appl. Surf. Sci. 256 (2010) 6284–6290.
[31] Y.P. Yan, S.R. Zhou, S. Liu, Atomistic simulation on nanomechanical response of indented graphene/nickel system, Comput. Mater. Sci. 130 (2017) 16–20.
[32] A. Stukowski, Visualization and analysis of atomistic simulation data with OVITO–the Open Visualization Tool, Model. Simul, Mater. Sci. Eng. 18 (2009), 015012.
[33] K. Durst, O. Franke, A. Böhner, M. Göken, Indentation size effect in Ni–Fe solid solutions, Acta Materialia 55 (20) (2007) 6825–6833, https://doi.org/10.1016/j.actamat.2007.08.044.
[34] A. Stukowski, Size effect and atomistic deformation mechanisms of hierarchically nanotwinned fcc metals under nanoindentation, J. Mater. Sci. 50 (2015) 7557–7567.
[35] T. Fu, X.H. Peng, X. Chen, S.Y. Weng, N. Hu, Q.B. Li, Z.C. Wang, Molecular dynamics simulation of nanoindentation on Cu/Ni nanotwinned multilayer films using a spherical indenter, Sci. Rep. 6 (2016) 35665.
[36] S. Tixier, P. Böni, H. Van Swygenhoven, Hardness enhancement of sputtered Ni 3 Al/Ni multilayers, Thin Solid Films 342 (1-2) (1999) 188–193, https://doi.org/10.1016/S0040-6090(98)01495-3.
[37] W.W. Jian, G.M. Cheng, W.Z. Xu, H. Yuan, M.H. Tsai, Q.D. Wang, C.C. Koch, Y. T. Zhu, S.N. Mathaudhu, Ultrastrong Mg alloy via nano-spaced stacking faults, Mater. Res. Lett. 1 (2013) 61–66.
[38] Q.M. Peng, Y. Sun, B.C. Ge, H. Fu, Q. Zu, X.Z. Tang, J.Y. Huang, Interactive contraction nanotwins-stacking faults strengthening mechanism of Mg alloys, Acta Mater. 169 (2019) 36–44.
[39] W.W. Jian, G.M. Cheng, W.Z. Xu, C.C. Koch, Q.D. Wang, Y.T. Zhu, S.N. Mathaudhu, Physics and model of strengthening by parallel stacking faults, Appl. Phys. Lett. 103 (2013), 133108.
[40] J. Wang, Y.G. Shen, F. Song, F.J. Ke, Y.L. Bai, C.S. Lu, Materials can be strengthened by nanoscale stacking faults, Europhys. Lett. 110 (2015) 36002.